Article

Magnetic Nanocarriers for pH/GSH/NIR Triple-Responsive Drug Release and Synergistic Therapy in Tumor Cells

Di Zhang, Wanyu Wei, Tianxiang Xie, Xue Zhou, Xu He, Jie Qiao, Rui Guo,* Gang Jin,* and Ningbo Li*

Read Online

ACCESS | Metrics & More | Article Recommendations | Supporting Information

ABSTRACT: In this study, the mesoporous Fe_3O_4 nanodrug carriers containing disulfide bonds (CHO-SMNPs) were successfully synthesized and characterized. Doxorubicin (DOX) was loaded onto the CHO-SMNPs as a model drug and gatekeeper through the formation of imine bonds with the aldehyde groups on the surface of the mesoporous materials. This drug carrier demonstrates effective drug release triggered by pH, glutathione (GSH), and near-infrared (NIR) light, along with satisfactory photothermal conversion efficiency under NIR irradiation at 808 nm. Furthermore, CHO-SMNPs exhibit excellent blood compatibility and biodegradability. They also show good biocompatibility and efficient cellular uptake in HeLa and MCF-7 cancer cells. Most importantly, the CHO-SMNPs/DOX has shown significant effectiveness in killing both HeLa and MCF-7 cancer cells. Consequently, CHO-SMNPs/DOX presents substantial potential as a magnetic-targeted, pH/GSH/NIR triple-triggered drug delivery system for synergistic chemo-photothermal therapy in tumor treatment.
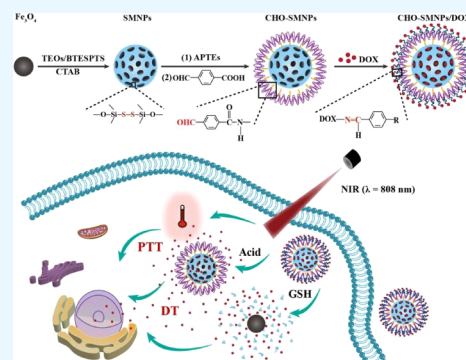
1. INTRODUCTION

Over the past decade, the incidence of tumors has steadily increased, presenting a significant threat to human health and well-being.[1] Chemotherapy remains the primary treatment approach for cancer; however, its effectiveness is often hindered by substantial side effects. Key challenges include the poor water solubility of many anticancer drugs, limited circulation time in the bloodstream, severe adverse reactions, a lack of treatment selectivity, and insufficient tissue penetration.[2−4] These issues underscore the need for innovative strategies to enhance the efficacy and safety of cancer therapies.

In recent years, the development of multifunctional nanodrug carriers has become an effective and popular strategy[5,6] for overcoming the challenges of nonselective drug delivery, low cellular uptake efficiency, and the side effects of traditional chemotherapy. Among these carriers, carbon-based nanomaterials have emerged as a promising platform for theranostics.[7] Additionally, mesoporous silicon nanoparticles (MSNs) are notable for their distinctive advantages.[8] MSNs can adopt various shapes, feature adjustable pore sizes, possess a large specific surface area, allow for easy surface modification, and exhibit excellent biocompatibility.[9−13] As a result, MSNs have emerged as promising candidates for diverse applications, including molecular imaging,[14] catalysis,[15] separation,[16] and drug delivery.[17,18] However, despite these benefits, MSNs face significant challenges related to poor degradability and the lack of targeted drug delivery capabilities.[19,20] To address these limitations, researchers are exploring hybrid silica carriers

incorporating S−S bonds within the Si−O−Si framework. This approach enables rapid redox-responsive biodegradation and enhances controlled release performance, paving the way for more effective and safer cancer treatments.[21,22]

To achieve controllable drug release, "smart" nanoparticles offer innovative possibilities for cancer therapy. Among these, pH-responsive gated nanomaterial carriers are particularly effective in providing regulated drug delivery.[23−25] However, the integration of auxiliary capping agents, such as ZnO and $Ca_3(PO_4)_2$, is often necessary in the current systems of pH-responsive and gated mesoporous silica nanoparticles.[26−28] Despite their utility, the potential risks associated with these "gatekeepers" have not been thoroughly evaluated. Moreover, drug carriers frequently face premature release of their therapeutic agents before reaching the tumor site, which can inadvertently damage healthy tissues.[29] Consequently, it is crucial to consider both the potential hazards posed by gating materials and the need to minimize drug release before arrival at the tumor. Thus, our approach to designing drug-carrying systems focuses not only on mitigating risks but also on

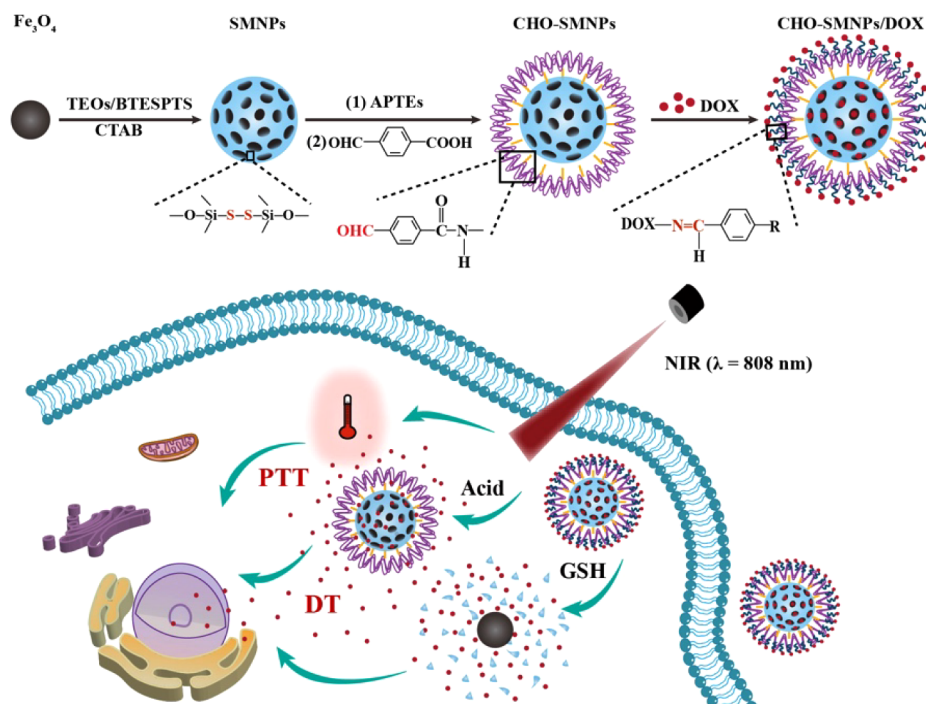**Scheme 1. Synthesis of pH/GSH/NIR Triple-Triggered Drug Carrier and Drug Release**

optimizing delivery to ensure that drugs remain effective and targeted.

Photothermal therapy (PTT) has emerged as a promising cancer treatment method, offering several advantages, such as minimal tissue invasion, high selectivity, and effective treatment with limited damage to surrounding healthy tissue.[30,31] Magnetic nanomaterials have attracted considerable interest in the biomedical field due to their superparamagnetic properties, excellent biocompatibility, and biodegradability.[32] For example, Fe_3O_4 nanomaterials demonstrate strong absorption of near-infrared (NIR) light and can facilitate photothermal conversion for effective cancer treatment.[33] Building on this, we propose utilizing mesoporous silicon nanoparticles coated with disulfide bonds to encase Fe_3O_4 nanomaterials, serving as a drug carrier. This approach aims to provide biodegradability, targeting capabilities, and the benefits of photothermal therapy. Additionally, doxorubicin (DOX) will be employed as a model drug and gatekeeper to enable controlled release of therapeutic agents, enhancing the treatment's efficacy while minimizing side effects.

In this study, we successfully synthesized a disulfide bond-doped mesoporous Fe_3O_4 nanodrug carrier, termed CHO-SMNPs, which responds to pH, glutathione (GSH), and near-infrared (NIR) light. This carrier demonstrates excellent drug loading capacity, stability, photothermal conversion efficiency, biocompatibility, and biodegradability while minimizing the side effects associated with premature drug release (Scheme 1). The synthesis began with the preparation of mesoporous silica-coated Fe_3O_4 nanomaterials (SMNPs) embedded with disulfide bonds, which were later functionalized with aldehyde groups. To showcase the functionality of our carrier, we selected DOX as a model drug. DOX, which contains amino groups, acts as a gatekeeper by forming imine bonds with the aldehyde groups on the carrier. This allows for the selective release of DOX under the weakly acidic conditions typical of tumor tissues, due to pH-induced imidohydrolysis. Further-

more, the CHO-SMNPs demonstrated sensitivity to the reducing agent glutathione (GSH), enabling the breakdown of disulfide bonds and subsequent drug release at high GSH concentrations (10 mM). Additionally, exposure to NIR light (808 nm) induced a photothermal effect that enhanced drug release and provided therapeutic benefits. Comprehensive in vitro loading and release tests, along with assessments of antitumor efficacy and biosafety, were conducted. These findings indicate that CHO-SMNPs/DOX holds promise as an advanced, targeted drug delivery system for synergistic chemo-photothermal therapy in tumor treatment.

2. MATERIALS AND METHODS

2.1. Materials and Instruments. Ferric chloride hexahydrate ($FeCl_3 \cdot 6H_2O$), sodium salicylate (NaSal), and Bis[3-(triethoxysilyl)propyl] tetrasulfide (BTESPTs) were purchased from Bailingway Technology Co. Ltd. Sodium acetate anhydrous (NaOAc), trisodium citrate, tetraethyl silicate (TEOs), ethylene glycol (EG), (3-aminopropyl)triethoxysilane (APTEs), dimethyl sulfoxide (DMSO), N-hydroxysuccinimide (NHS), 1-(3-(dimethylamino)propyl)-3-ethylcarbodiimide hydrochloride (EDC), doxorubicin hydrochloride (DOX·HCl), cetyltrimethylammonium bromide (CTAB) were purchased from Shanghai Aladdin Reagent Co., Ltd. Calcein acetoxymethyl ester (calcein-AM), 4′,6-diamidino-2-phenylindole (DAPI) and propidium iodide (PI) were obtained from Boster Biological Technology Co. Ltd. Other chemicals were purchased from Tianjin Damao Chemical Reagent Co. Ltd. Cell Counting Kit-8 (CCK-8) was provided by Beyotiome Biotechnology Co. Ltd.

TEM images were captured using a JEM-2100 transmission electron microscope (Tokyo, Japan). UV−vis spectra measurements were carried out on a UH5300 UV−vis spectrophotometer (Tokyo, Japan). Fourier transform infrared (FTIR) spectroscopy was measured on a BRUKER FTIR spectrometer (Bruker, Germany). X-ray diffraction (XRD) patterns were
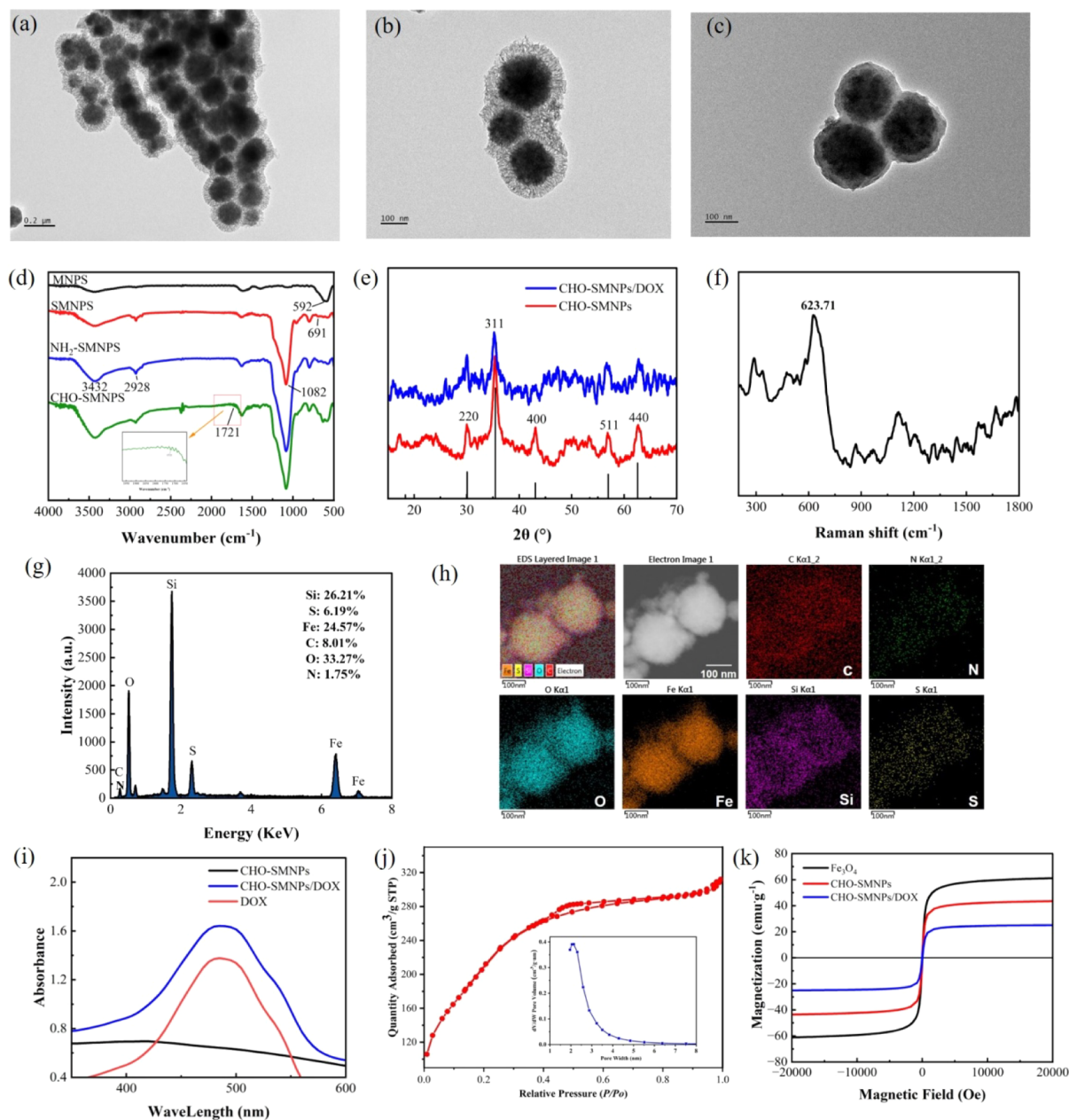
Figure 1. TEM images of the (a) SMNPs, (b) CHO-SMNPs, and (c) CHO-SMNPs/DOX; (d) FTIR spectra of MNPs, SMNPs, CHO-SMNPs, and CHO-SMNPs/DOX; (e) X-ray diffraction patterns of CHO-SMNPs and CHO-SMNPs/DOX; (f) The Raman spectra of CHO-SMNPs; (g) The EDS spectra of CHO-SMNPs; (h) Mapping images of CHO-SMNPs; (i) The UV−vis absorption spectrum for DOX, CHO-SMNPs and CHO-SMNPs/DOX; (j) Nitrogen adsorption−desorption isotherm of CHO-SMNPs. Inset: the pore size distribution; (k) Magnetization curves of MNPs, CHO-SMNPs and CHO-SMNPs/DOX.

obtained using a diffractometer (PANALY) with Cu−Kα radiation ($\lambda = 1.5405$ Å) and the powder samples were scanned in the 2θ angle range from $10°$ to $80°$. Nitrogen sorption instrument (Bester Beijing Instrument Company, 3H-2000PS2, China) was used to detect the Brunauer-Emmet-Teller (BET) specific surface area. The magnetic properties were measured using a SQUID vibrating sample magnetometer (VSM) (Quantum Design). The magnetization curves were recorded at 300 K with a magnetic field cycled between −20,000 and 20,000 G. Fluorescence images were captured using a Nikon Eclipse Ti2 inverted fluorescence microscope (Tokyo, Japan).

2.2. Preparation of MNPs and SMNPs. Fe_3O_4 nano-particles (MNPs) were prepared via the solvothermal method

as described with slight modifications.[38] SMNPs were synthesized using the reported method.[34] The full protocol is detailed in the Supporting Information.

2.3. Preparation of CHO-SMNPs. To prepare NH_2−SMNPs, 120 mg of SMNPs were dissolved in 20 mL of toluene and agitated at 30 °C for 1 h. Then, 200 μL of APTEs was added dropwise, and the mixture was refluxed for 24 h to functionalize the SMNPs with amino groups. The product NH_2−SMNPs was separated by hysteresis and washed three times with ethanol.

For CHO-SMNPs, 0.60 g of NH_2−SMNPs and 30 mg of 4-formylbenzoic acid were dissolved in a 20 mL solution of deionized water and DMSO (4:1 v/v). After adding 46 mg of EDC and 27.6 mg of NHS to activate the carboxyl groups, the
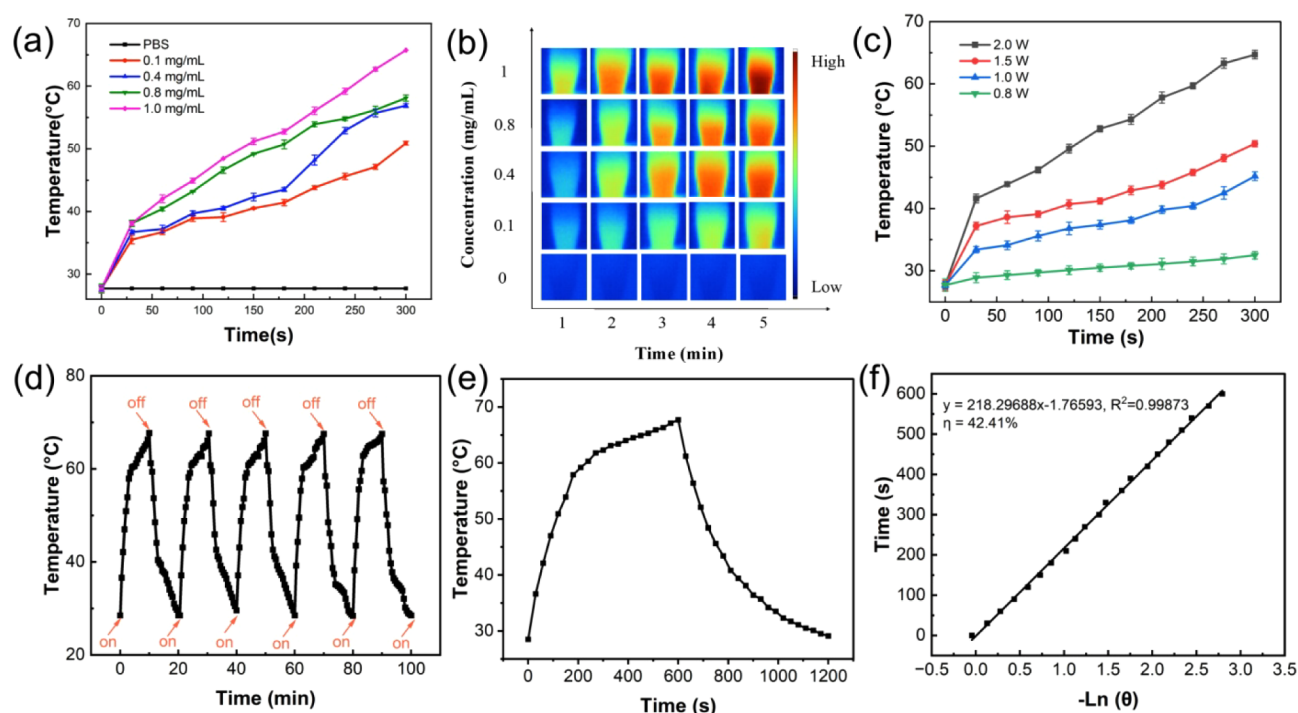
Figure 2. (a) Temperature change curves; (b) The corresponding infrared thermal images of CHO-SMNPs solutions with different concentrations; (c) Temperature-increase curve of CHO-SMNPs irradiated with different laser irradiation intensities (808 nm); (d) Temperature variation curve of laser on/off cycles; (e, f) Calculation of photothermal conversion efficiency.

mixture was agitated for 24 h at room temperature. The resulting product was separated by hysteresis, washed three times with ethanol, and vacuum-dried at 30 °C for 24 h to obtain CHO-SMNPs.

2.4. Drug Loading and Releasing Performance of CHO-SMNPs. *2.4.1. DOX Standard Curve.* Experimental details are provided in the Supporting Information.

2.4.2. Preparation of CHO-SMNPs/DOX. 50 mg of CHO-SMNPs and 25 mg of DOX were separately dispersed in 28 and 12 mL of DI water (pH 6.0) using ultrasound. The suspensions were mixed and shaken at 200 rpm for 24 h at 37 °C in the dark. The resulting CHO-SMNPs/DOX product was collected via centrifugation, and the supernatant was analyzed with a UV−vis spectrophotometer at 480 nm to determine drug encapsulation efficiency. Subsequently, the product was capped with DOX through a reversible covalent benzoic-imine linkage at pH 8.5. After additional centrifugation and three washes with DI water, the final product was freeze-dried for 24 h and designated as CHO-SMNPs/DOX.

2.4.3. Drug Releasing Performance of DOX on CHO-SMNPs. In the drug release experiment, 10 mg of CHO-SMNPs/DOX was dispersed in 25 mL of PBS and divided into five groups: (1) pH 7.4 & GSH 0 mM; (2) pH 5.5 & GSH 0 mM; (3) pH 7.4 & GSH 10 mM; (4) pH 5.5 & GSH 5 mM; and (5) pH 5.5 & GSH 10 mM. The samples were shaken at 200 rpm and 37 °C in the dark. At regular intervals, supernatants were collected after centrifugation, and DOX concentrations were determined by measuring absorbance at 480 nm using a DOX standard curve. Additionally, to assess the effect of NIR on DOX release, one group was irradiated with NIR (808 nm, 2.0 W/cm²) for 5 min at various time points, while the other served as a control without NIR exposure.

2.5. The Photothermal Conversion Efficiency of CHO-SMNPs. (1) CHO-SMNPs suspensions at concentrations of 0.1, 0.4, 0.8, and 1.0 mg/mL, along with PBS, were irradiated with an NIR laser (808 nm, 2.0 W/cm²) for 0−5 min, and infrared thermal images were captured. (2) A 1.0 mg/mL CHO-SMNPs suspension was irradiated with an 808 nm laser at varying power densities (0.5, 1.0, 1.5, 2.0 W/cm²) for 5 min. (3) The 1.0 mg/mL CHO-SMNPs suspension underwent five 20 min laser on−off cycles at a power density of 2.0 W/cm², cooling to 28.5 °C between cycles. Temperature measurements were taken every 30 s with an infrared thermal imager in a controlled room temperature of 23 °C.

2.6. Antitumor Activity of CHO-SMNPs/DOX In Vitro. *2.6.1. Cytotoxicity In Vitro.* Cell viability was assessed using the Cell Counting Kit-8 (CCK-8). MCF-7, HeLa, and HUVEC cells (5×10^4 cells/well) were seeded in 96-well plates and incubated for 24 h at 37 °C. The adhered cells were then coincubated with NH_2-MMNPs or oMMNPs/DOX at concentrations of 1, 5, 10, 30, 50, and 70 μg/mL (DOX equivalent: 0.03−0.20 μg/mL). Cells were irradiated with NIR (808 nm, 2.0 W/cm²) for 5 min and incubated at 37 °C for 20 h. After adding the CCK-8 reagent, the cells were incubated for an additional 4 h, and absorbance was measured at 450 nm using an enzyme-linked immunoassay instrument.

2.6.2. Apoptosis Assay. HeLa cells were treated to investigate the effects of CHO-SMNPs and CHO-SMNPs/DOX as a synergistic therapy. Nanoparticles at 30 μg/mL (DOX concentration: 0.4 μg/mL) were applied to each experimental group, while control groups were cultured in PBS. The PTT and CT/PTT groups were coincubated for 6 h and then subjected to 5 min of laser irradiation (808 nm, 2 W/cm²). After staining all groups with calcein-AM and PI, cells were incubated in the dark for 30 min and observed under a fluorescent microscope before imaging.
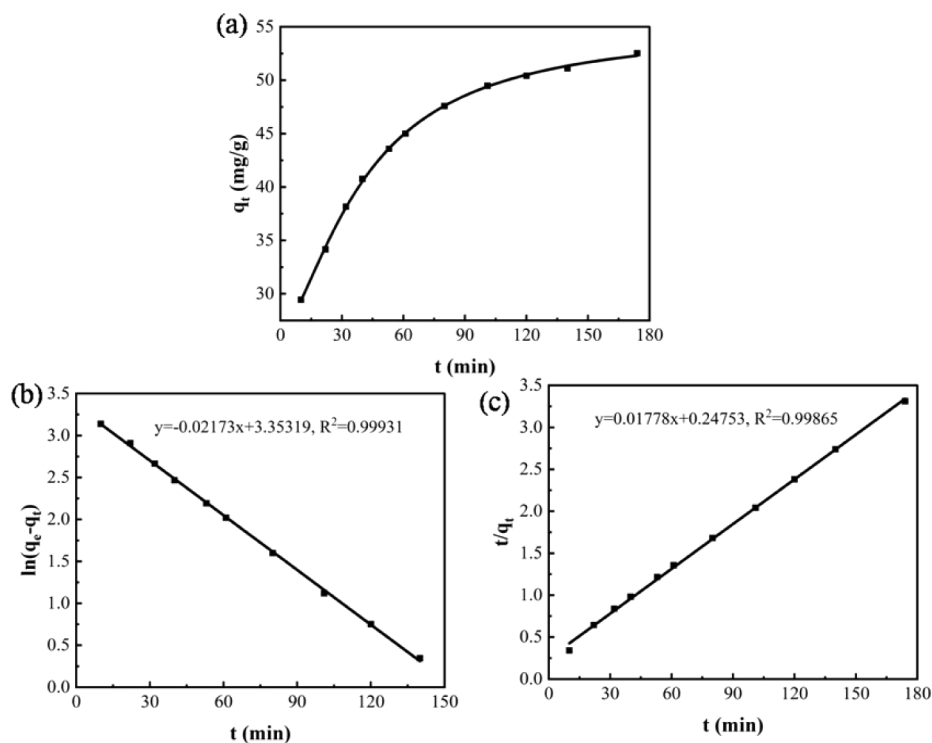
Figure 3. (a) The adsorption kinetics curve of DOX on CHO-SMNPs; (b) Line fittings of the dynamic model for Lagergren's pseudo-first-order and (c) Ho's pseudo-second-order.
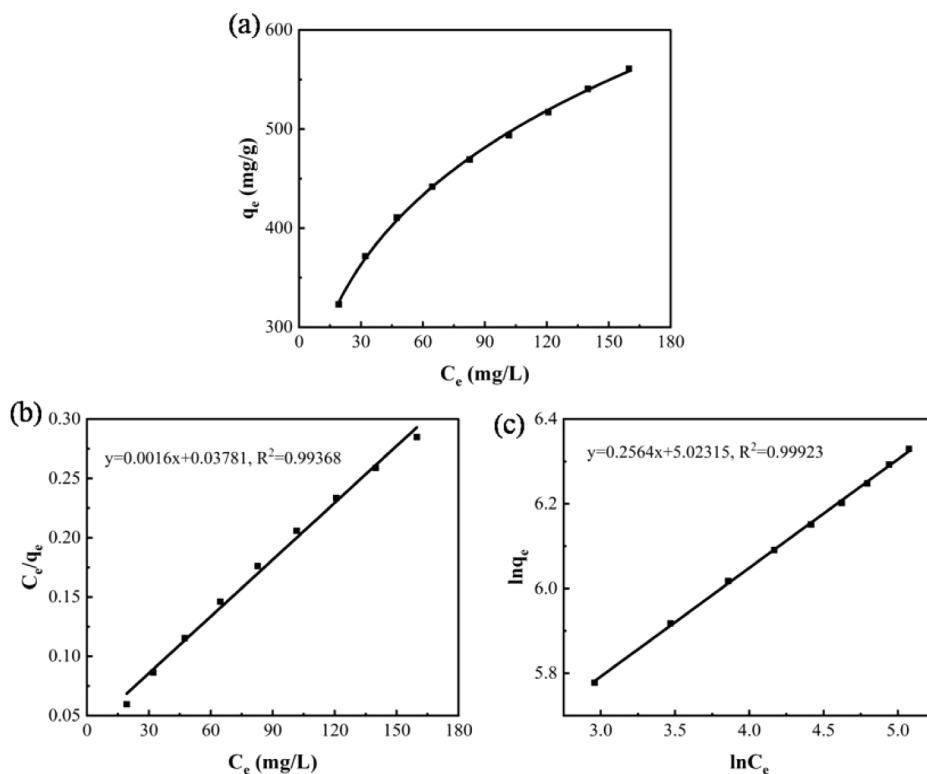

Figure 4. (a) The adsorption isotherm curve of DOX on CHO-SMNPs. Linear fitting graphs with the Langmuir adsorption isotherm model (b) and Freundlich adsorption isotherm model (c).

2.6.3. Cellular Uptake. HeLa and MCF-7 cells were seeded in a 96-well plate at a density of 5×10^4 cells per well and incubated for 12 h. The medium was then replaced: the experimental group received CHO-SMNPs/DOX, while the control group was maintained in an untreated medium. After another 12 h, DAPI staining was performed. The medium was aspirated, and cells were washed three times with PBS. They were fixed with 4% paraformaldehyde (PFA) for 2 h and
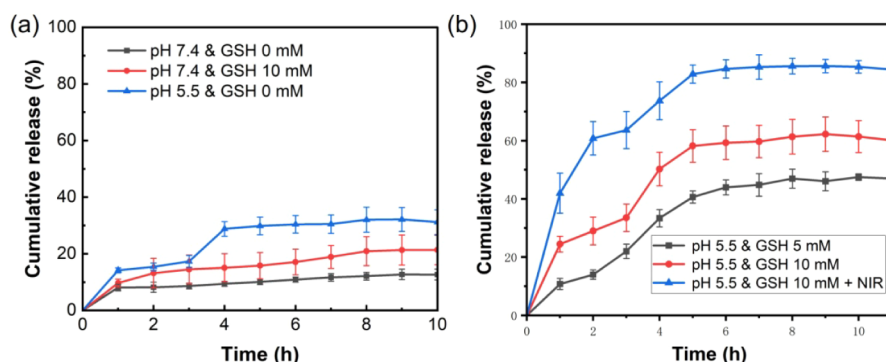
Figure 5. (a) Release profiles of CHO-SMNPs/DOX in PBS buffer of different pH and GSH; (b) The cumulative release of CHO-SMNPs/DOX in PBS buffer of pH = 5.5 and GSH = 5.0, 10 mM and pH = 5.5 and GSH = 10 mM + NIR.
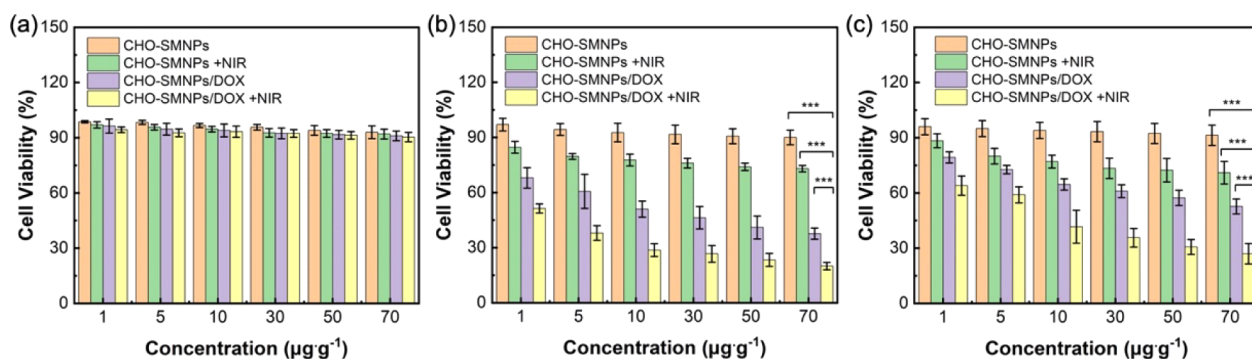

Figure 6. Cell viabilities of HUVEC (a), HeLa (b), and MCF-7 (c) cells incubated with varied concentrations (1−70 μg/mL) of CHO-SMNPs or CHO-SMNPs/DOX (the equivalent DOX concentration is 0.1 to 0.9 μg/mL) with or without laser irradiation.***$p < 0.001$.

washed again three times with PBS. Cells were then treated with Triton X-100 for 20 min, washed three times with PBS, and stained with 1% DAPI for 20 min followed by three PBS washes. Imaging was performed using confocal laser scanning microscopy (CLSM), and the cellular uptake of CHO-SMNPs/DOX was assessed via flow cytometry.

3. RESULTS AND DISCUSSION

3.1. Characterization of the CHO-SMNPs and CHO-SMNPs/DOX. Figure 1a−c presents the transmission electron
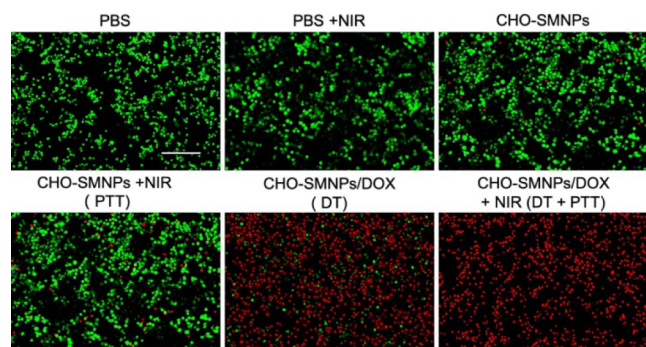

Figure 7. Fluorescence images of calcein-AM and PI colabeled HeLa cells after varied treatments (scale bar, 100 μm).

microscopy (TEM) images of SMNPs, CHO-SMNPs, and CHO-SMNPs/DOX, as well as the particle size distributions of CHO-SMNPs (Figure S1). The TEM images reveal that the SMNPs and CHO-SMNPs exhibit a uniform spherical shape with visible dendritic pores, indicating good dispersion. The

silicon dioxide layer on the nanoparticles has a thickness of approximately 20 nm (Figure 1a,b). Compared to the unmodified magnetic nanomaterials previously reported by Qi et al.,[35] the dispersion of Fe_3O_4 in the CHO-SMNPs is significantly improved. Following successful drug loading, the pore structures become less distinct (Figure 1b), confirming the successful loading of the drug DOX onto the nanomaterials. The CHO-SMNPs sample displays uniform spherical particles with a size of 210 nm with a polymer dispersity Index of 0.142 (Figure 1c), indicating good dispersion.

As shown in the FTIR spectra in Figure 1d, it can be seen that 592 cm^{-1} is the stretching vibration peak of the Fe−O bond, which is the characteristic absorption peak of Fe_3O_4. After the functionalization of nanoparticles, the corresponding peaks were also observed in infrared spectra. Among them, the strong peak at 691 cm^{-1} belonged to the stretching vibration of the C−S bond, and the Si−O−Si stretching vibration peak was at 1082 cm^{-1},[36−38] which indicates that SiO_2 containing −S-S- successfully coated Fe_3O_4. Also, the broad absorption peak at 3432 cm^{-1} corresponds to the stretching vibration peak of O−H or N−H, and the stretching vibration peak of C−H is 2928 cm^{-1}, which indicates that amino groups have been successfully introduced into the surface of the material. In addition, the stretching vibration peak of the benzaldehyde C=O bond is at 1721 cm^{-1}, which indicates that the aldehyde group is successfully introduced on the surface of the material. Figure 1e shows XRD patterns of CHO-SMNPs and CHO-SMNPs/DOX samples. Both samples show sharp diffraction peaks at 2θ = 30.6°, 35.99°, 43.71°, 57.71° and 63.28°, which are assigned to the (220), (311), (400), (511), and (440) crystal planes, respectively, of Fe_3O_4 according to standard card JCPDS NO. 85-1436. A prominent peak at 23° is
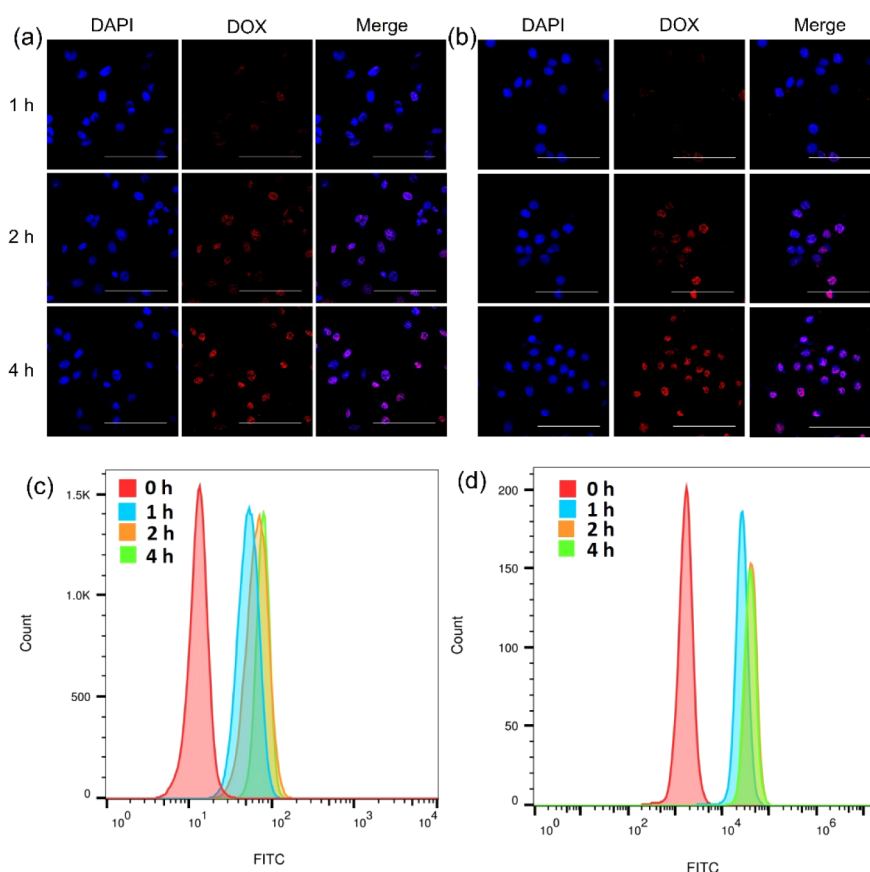
Figure 8. Confocal laser scanning microscope (CLSM) of CHO-SMNPs/DOX incubated with HeLa (a) and MCF-7 (b) cells for 1 h, 2 and 4 h (Scale bar, 100 μm). The uptake of CHO-SMNPs/DOX by HeLa (c) and MCF-7 cells (d) was detected by flow cytometry.

observed in the XRD patterns of both samples, which is attributed to the SiO$_2$ shell that is coated on the Fe$_3$O$_4$ nanoparticles. As shown in Figure 1f, the Raman spectrum of CHO-SMNP carriers exhibits a stretching vibration peak at 623.71 cm^{-1}, which confirms the presence of S−S bonds.[21] Additionally, the EDS spectrum and mapping images (Figure 1g,h) reveal the presence of Fe, Si, O, C, N, and S elements in the CHO-SMNPs. Additionally, the EDS data suggests approximately 6.19% sulfur doping in the nanoparticles.

In addition, after loading DOX into CHO-SMNPs, a significant DOX absorption peak appeared at 480 nm (Figure 1i), indicating that DOX has been successfully loaded into the particle structure.[39] Furthermore, the pore size distribution and surface area ratio of the CHO-SMNP nanoparticles were determined through analysis of the N$_2$ adsorption curves (Figure 1j). The results demonstrated a type IV isotherm, confirming a homogeneous and narrow mesoporous size distribution. The surface area was measured to be 718.27 m^2/g, with an average mesopore diameter of 2.42 nm. Figure 1k depicts the magnetization characterization of MNPs, CHO-SMNPs, and CHO-SMNPs/DOX at room temperature. The saturation magnetizations (Ms) of MNPs, CHO-SMNPs, and CHO-SMNPs/DOX are approximately 61.09, 43.49, and 25.03 emu/g, respectively, which confirms potential use as a magnetically targeted drug.

3.2. The Photothermal Conversion Efficiency of CHO-SMNPs. The concentration-dependent photothermal effect and stability of CHO-SMNPs were investigated using an infrared thermal imaging system. Temperature changes of the solutions were recorded under near-infrared irradiation (NIR)

with a wavelength of 808 nm. First, as illustrated in Figure 2a, the CHO-SMNPs solutions with various concentrations (0 mg/mL to 1.0 mg/mL) were illuminated with an NIR laser (2.0 W/cm^2) for 5 min and the temperature heated from 27.7 to 64.7 °C. The results showed that the photothermal conversion efficiency of the CHO-SMNPs increased with increasing concentration. Infrared thermal images displayed in Figure 2b corresponded to those shown in Figure 2a and demonstrated the strong photothermal action of the material. Furthermore, the photothermal conversion efficiency of CHO-SMNPs was found to be dependent on the laser power intensity, as shown in Figure 2c. When the NIR laser irradiation intensity was increased from 0.5 W/cm^2 to 2.0 W/cm^2, the temperature of the CHO-SMNP solution at the same concentration increased significantly from 32.5 to 64.7 °C. Further evidence of their exceptional photothermal stability was demonstrated by the unaltered temperature profiles in Figure 2d after undergoing five heating and cooling cycles.[40] The photothermal conversion efficiency was calculated to be 42.41% (Figure 2e,f). In contrast to mesoporous bioglass nanoparticles based on carbon dots, CHO-SMNPs exhibit superior NIR photothermal conversion performance, exceeding the approximately 32.4% efficiency reported by Singh et al.[41] This enhancement broadens the potential applications of CHO-SMNPs in photothermal therapy.

3.3. Blood Compatibility and Stability. The prerequisite for preventing hemolysis of the nanodrug delivery carrier during blood circulation following intravenous injection is good blood compatibility. The results of the hemolysis test for CHO-SMNPs and CHO-SMNPs/DOX are shown in Figure

S2. Comparing the CHO-SMNPs and CHO-SMNPs/DOX group to the negative control group, the hemolysis percentages (eq S1) and hemolysis images showed that, within a certain concentration range (0.1−0.3 mg/mL), there was no obvious hemolysis phenomenon. This indicated that our synthetic CHO-SMNPs and CHO-SMNPs/DOX had excellent blood compatibility and could ensure their safe delivery into the body.

3.4. Drug Loading Efficiency of CHO-SMNPs.

Figure S3 shows the UV−vis absorption spectrum of DOX. It is evident from the figure that various DOX concentrations exhibit a maximum absorption peak at 480 nm. Therefore, the 480 nm ultraviolet wavelength was chosen to construct the standard curve and assess its drug loading. Figure S4 displays the linear equation of DOX, which is A = 0.01591x + 0.01814 (R^2 = 0.99914), within the range of 5−55 μg/mL.

The nanomaterials were loaded with DOX through physical adsorption and chemical covalent bonding. Figure 3a presents the adsorption kinetics curve of DOX by CHO-SMNPs. The figure clearly shows that the loading of the anticancer drug DOX by the CHO-SMNPs nanomaterial can be divided into three stages. Initially, during the first 60 min, DOX is rapidly loaded by the nanomaterial. Subsequently, the loading rate gradually slows down between 60 and 120 min. Finally, after 3 h, the drug loading reaches saturation (eq S2). In addition, Lagergren's pseudo-first-order kinetic model (eq S4) and Ho's pseudo-second-order kinetic model (eq S5) were used to further study the adsorption mechanism. Figure 3b,c exhibits the linear relationship obtained using the quasi-primary and quasi-secondary kinetic equations, respectively. These relationships portray the drug loading time (t) as the horizontal coordinate and $\ln(q_e-q_t)$ and t/q_t as the vertical coordinates. The plots, in conjunction with Table S1, demonstrate that the loading process of DOX by the CHO-SMNPs nanomaterial involves both physical and chemical adsorption.

Whereafter, the adsorption isotherm of CHO-SMNPs for DOX was investigated. As shown in Figure 4a, with the increase in DOX concentration, the drug loading of DOX by CHO-SMNPs gradually increased. At a concentration of 300 mg/L, the maximum DOX loading capacity was 567 mg/g (eq S3). We measured the drug loading efficiency and encapsulation efficiency as 54.32% and 88.02% by UV−Vis, respectively (eqs S8 and S9). To analyze and discuss the drug loading of CHO-SMNPs, the single-layer Langmuir (eq S6) and multilayer Freundlich (eq S7) isothermal adsorption models were employed, with C_e and $\ln C_e$ as the horizontal coordinates and C_e/q_e and $\ln q_e$ as the vertical coordinates, respectively. As depicted in Figure 4b,c and summarized in Table S2, Figure 4c provides a better reflection of the drug loading mechanism of nanomaterials compared to Figure 4b. Moreover, the correlation coefficient R_c^2 (0.99923) for Figure 4c is higher than R_b^2 (0.99368) in Figure 4b, which indicates that the drug loading process of CHO-SMNPs for DOX aligns more closely with the Freundlich adsorption model. Therefore, it can be inferred that the primary driving force for drug loading is multimolecular layer adsorption, in addition to monolayer adsorption.

Given that the tumor cell microenvironment differs from that of normal cells,[18] the release behaviors of DOX from CHO-SMNPs were investigated in different pH levels and GHS concentrations (eq S10). The results presented in Figure 5 depict the kinetic release profiles of DOX from the CHO-SMNPs/DOX when exposed to NIR (2.0 W/cm²) and GSH

concentrations of 0 mM, 5 mM, and 10 mM, in 0.1 M PBS at different pH levels (5.5 and 7.4). It can be seen that the drug release rate increases with the decrease in pH and the increase in GHS concentration. Notably, at pH 5.5 with GSH 10 mM (2.0 W/cm²), DOX release was observed to reach a cumulative percentage of 84.25% after 8 h (Figure 5b). Conversely, under the same conditions, DOX release was only 13.71% at pH 7.4 with GSH 0 mM (Figure 5a). These findings suggest that the CHO-SMNPs/DOX nanoparticles exhibit a release behavior that is sensitive to both pH and GSH. Compared with the reported nanocarriers.[42] This drug delivery system demonstrates superior performance in both drug loading and release. In addition, NIR also played a crucial role in drug release, offering a promising approach for the cotreatment of tumors through chemo-photothermal therapy.[43]

3.5. Antitumor Activity of CHO-SMNPs/DOX In Vitro.

3.5.1. Cytotoxicity Test. To demonstrate that the CHO-SMNPs were advantageous, we adopted the Cell Counting Kit-8 (CCK-8) assay to compare the toxic effects of CHO-SMNPs and CHO-SMNPs/DOX on HUVEC cells (a), HeLa cells (b), and MCF-7 cells (c) (Figure 6). It could be seen that the cell survival rates of the CHO-SMNPs and CHO-SMNPs + NIR groups alone were around 94%, indicating the high biocompatibility and low cytotoxicity of CHO-SMNPs. However, the cytotoxicity of both types of cancer cells increased with the concentration of CHO-SMNPs/DOX and displayed concentration-dependent behavior. At a concentration of 10 μg/mL combined with NIR (2.0 W/cm²), approximately 63.33% of HeLa cells and 60.33% of MCF-7 cells were found to have died after 24 h. These findings indicate that CHO-SMNPs meet the requirements for drug delivery systems and show potential for various applications.

3.5.2. Cell Apoptosis Assay. To examine the killing effects of chemo-photothermal therapy in vitro, HeLa cancer cells were incubated with CHO-SMNPs or CHO-SMNPs/DOX (DOX concentration is 0.4 μg/mL) nanoparticles and irradiated with an NIR laser. As shown in Figure 7, the use of NIR (808 nm 2.0 W/cm²) to incubate CHO-SMNPs for 5 min resulted in the photothermal therapy (PTT) effect, leading to the production of some dead cells. The combined effect of chemotherapy (CT) and PTT in the CHO-SMNPs/DOX group with laser irradiation showed the lowest cell survival rate. These findings indicate that the synergistic effect of CT and PTT significantly enhances the tumor cell-killing capability of CHO-SMNPs/DOX.

3.5.3. Cellular Uptake. Finally, confocal laser scanning microscopy (CLSM) was utilized to observe the uptake of DOX-loaded CHO-SMNPs. As shown in Figure 8, upon incubation with CHO-SMNPs/DOX for 1 h, a strong red fluorescence indicative of DOX molecules was observed in the nuclei of HeLa (a) and MCF-7 (b) cells. The number of cells exhibiting this red fluorescence gradually increased over time, and the intensity of the red fluorescence was high. These observations suggest that the uptake of CHO-SMNPs/DOX by cells increases with incubation time, demonstrating the efficient delivery and release of DOX by CHO-SMNPs within the cells. Additionally, the cellular uptake of CHO-SMNPs/DOX was assessed using flow cytometry analysis (Figure 8c,d). The results indicated that CHO-SMNPs/DOX was nearly completely taken up by both types of cancer cells after 2 h, corroborating the findings from CLSM images.

4. CONCLUSIONS

In summary, the biodegradable disulfide bond doped mesoporous magnetic nanomaterials (CHO-SMNPs) were successfully synthesized. The resulting CHO-SMNPs/DOX possesses the following advantages: (1) high loading efficiency of DOX for chemotherapy; (2) pH/GSH/NIR triple-triggered drug release; (3) excellent photothermal conversion efficiency for photothermal therapy; (4) uniform sulfur doping combined with a self-gating mechanism for DOX that minimizes burst release; and (6) outstanding biocompatibility and stability. The CHO-SMNPs/DOX nanodrugs have a strong antitumor impact in the in vitro trials with HeLa and MCF-7 cells, which is based on the synergistic effect of chemotherapy with the medication DOX and photothermal therapy with the CHO-SMNPs carrier. Future work will focus on more extensive in vivo evaluations to set these outcomes. Therefore, the synthesized CHO-SMNPs/DOX has the potential to be utilized in clinical settings for cotherapy of photothermal chemotherapy in the treatment of cancer. This advancement is expected to result in more comprehensive cancer diagnoses and improved treatment outcomes across various cancer types.

ASSOCIATED CONTENT

Ⓢ Supporting Information

The Supporting Information is available free of charge at https://pubs.acs.org/doi/10.1021/acsomega.4c08267.

> Details of preparation experiments of MNPs and SMNPs, the standard curve of DOX, blood compatibility, and stability, the adsorption kinetics and adsorption isotherm of CHO-SMNPs for DOX (PDF)

AUTHOR INFORMATION

Corresponding Authors

Rui Guo − *School of Basic Medical Sciences, Shanxi Medical University, Taiyuan 030001, China*; Email: ruiguo@sxmu.edu.cn

Gang Jin − *Department of Medical Oncology, Second Hospital of Shanxi Medical University, Taiyuan 030001, China*; Email: jingang2018@sina.com

Ningbo Li − *School of Basic Medical Sciences, Shanxi Medical University, Taiyuan 030001, China*; ⓘ orcid.org/0000-0002-7456-6272; Email: ningboli@sxmu.edu.cn

Authors

Di Zhang − *School of Basic Medical Sciences, Shanxi Medical University, Taiyuan 030001, China*

Wanyu Wei − *School of Basic Medical Sciences, Shanxi Medical University, Taiyuan 030001, China*

Tianxiang Xie − *School of Stomatology, Shanxi Medical University, Taiyuan 030001, China*

Xue Zhou − *School of Basic Medical Sciences, Shanxi Medical University, Taiyuan 030001, China*

Xu He − *School of Basic Medical Sciences, Shanxi Medical University, Taiyuan 030001, China*

Jie Qiao − *School of Basic Medical Sciences, Shanxi Medical University, Taiyuan 030001, China*

Complete contact information is available at:
https://pubs.acs.org/10.1021/acsomega.4c08267

Notes

The authors declare no competing financial interest.

ACKNOWLEDGMENTS

REFERENCES

(1) Sung, H.; Ferlay, J.; Siegel, R. L.; Laversanne, M.; Soerjomataram, I.; Jemal, A.; Bray, F. Global cancer statistics 2020: GLOBOCAN estimates of incidence and mortality worldwide for 36 cancers in 185 countries. *Ca-Cancer J. Clin.* **2021**, *71*, 209−249.

(2) Alhodieb, F. S.; Barkat, M. A.; Barkat, H. A.; Ab Hadi, H.; Khan, M. I.; Ashfaq, F.; Rahman, M. A.; Hassan, M. Z.; Alanezi, A. A. Chitosan-modified nanocarriers as carriers for anticancer drug delivery: Promises and hurdles. *Int. J. Biol. Macromol.* **2022**, *217*, 457−469.

(3) Feng, X. Y.; Li, F. S.; Zhang, L. L.; Liu, W. M.; Wang, X. P.; Zhu, R.; Qiao, Z. A.; Yu, B.; Yu, X. H. TRAIL-modified, doxorubicin-embedded periodic mesoporous organosilica nanoparticles for targeted drug delivery and efficient antitumor immunotherapy. *Acta Biomater.* **2022**, *143*, 392−405.

(4) Joseph, M. M.; Ramya, A. N.; Vijayan, V. M.; Nair, J. B.; Bastian, B. T.; Pillai, R. K.; Therakathinal, S. T.; Maiti, K. K. Targeted theranostic nano vehicle endorsed with self-destruction and immunostimulatory features to circumvent drug resistance and wipe-out tumor reinitiating cancer stem cells. *Small* **2020**, *16* (38), No. e2003309.

(5) Wang, T. Y.; Lei, H. L.; Li, X.; Yang, N. L.; Ma, C.; Li, G. Q.; Gao, X.; Ge, J.; Liu, Z.; Cheng, L.; Chen, G. Magnetic Targeting Nanocarriers Combined with Focusing Ultrasound for Enhanced Intracerebral Hemorrhage Therapy. *Small* **2023**, *19* (17), 2206982.

(6) Chen, D. Y.; Liu, X. C.; Lu, X. Y.; Tian, J. W. Nanoparticle drug delivery systems for synergistic delivery of tumor therapy. *Front. Pharmacol.* **2023**, *14*, 1111991.

(7) Patel, K. D.; Singh, R. K.; Kim, H. W. Carbon-based nanomaterials as an emerging platform for theranostics. *Mater. Horiz.* **2019**, *6*, 434.

(8) Singh, R. K.; Patel, K. D.; Leong, K. W.; Kim, H. W. Progress in Nanotheranostics Based on Mesoporous Silica Nanomaterial Platforms. *ACS Appl. Mater. Interfaces* **2017**, *9*, 10309.

(9) Živojević, K.; Mladenović, M.; Djisalov, M.; Mundzic, M.; Ruiz-Hernandez, E.; Gadjanski, I.; Knežević, N. Ž. Advanced mesoporous silica nanocarriers in cancer theranostics and gene editing applications. *J. Controlled Release* **2021**, *337*, 193−211.

(10) Fernandes, N. B.; Nayak, Y.; Garg, S.; Nayak, U. Y. Multifunctional engineered mesoporous silica/inorganic material hybrid nanoparticles: Theranostic perspectives. *Coord. Chem. Rev.* **2023**, *478*, 214977.

(11) Vallet-Regí, M.; Schüth, F.; Lozano, D.; Colilla, M.; Manzano, M. Engineering mesoporous silica nanoparticles for drug delivery: where are we after two decades. *Chem. Soc. Rev.* **2022**, *51*, 5365−5451.

(12) Manzano, M.; Vallet-Regí, M. Mesoporous silica nanoparticles for drug delivery. *Adv. Funct. Mater.* **2020**, *30*, 1902634.

(13) Zhou, S.; Zhong, Q.; Wang, Y.; Hu, P.; Zhong, W.; Huang, C. B.; Yu, Z. Q.; Ding, C. D.; Liu, H. X.; Fu, J. J. Chemically engineered mesoporous silica nanoparticles-based intelligent delivery systems for theranostic applications in multiple cancerous/non-cancerous diseases. *Coord. Chem. Rev.* **2022**, *452*, 214309.

(14) Jiang, Z. Y.; Zhang, M. H.; Li, P. F.; Wang, Y.; Fu, Q. R. Nanomaterial-based CT contrast agents and their applications in image-guided therapy. *Theranostics* **2023**, *13*, 483−509.

(15) Kumari, R.; Narvi, S.; Dutta, P. Synthesis of chitosan succinate-g-amine functionalized mesoporous silica: Inorganic-organic nano-hybrid for antibacterial assessment, antioxidant activity and pH-controlled drug delivery. *Int. J. Biol. Macromol.* **2023**, *234*, 123763.

(16) Lee, T. H.; Moghadam, F.; Jung, J. G.; Kim, Y. J.; Roh, J. S.; Yoo, S. Y.; Lee, B. K.; Kim, J. H.; Pinnau, I.; Park, H. B. In situ derived hybrid carbon molecular sieve membranes with tailored ultra-microporosity for efficient gas separation. *Small* **2021**, *17* (47), 2104698.

(17) Feng, Y.; Liao, Z.; Li, M. Y.; Zhang, H. X.; Li, T. T.; Qin, X.; Li, S.; Wu, C. H.; You, F. M.; Liao, X. L.; Cai, L. L.; Yang, H.; Liu, Y. Y. Mesoporous Silica Nanoparticles-Based Nanoplatforms: Basic Construction, Current State, and Emerging Applications in Anticancer Therapeutics. *Adv. Healthcare Mater.* **2023**, *12*, 2201884.

(18) Zhou, X.; He, X.; Dong, Z. Y.; Wang, Y. X.; Hu, C. Q.; Zhang, D.; Guo, R.; Qiao, J.; Li, N. B. Manganese-Doped Mesoporous Magnetic Nanocarriers for Cancer Treatment. *ACS Appl. Nano Mater.* **2024**, *7*, 6339−6350.

(19) Huang, L.; Liu, J.; Gao, F.; Cheng, Q.; Lu, B.; Zheng, H.; Xu, H. X.; Xu, P. H.; Zhang, X. Z.; Zeng, X. A dual-responsive, hyaluronic acid targeted drug delivery system based on hollow mesoporous silica nanoparticles for cancer therapy. *J. Mater. Chem. B* **2018**, *6*, 4618−4629.

(20) Sancho-Albero, M.; Rosso, G.; De Cola, L.; Cauda, V. Cargo-loaded lipid-shielded breakable organosilica nanocages for enhanced drug delivery. *Nanoscale* **2023**, *15*, 14628−14640.

(21) Li, X. L.; Chen, Y. Y.; Zhang, X.; Zhao, Y. B. Fabrication of biodegradable auto-fluorescent organosilica nanoparticles with dendritic mesoporous structures for pH/redox-responsive drug release. *Mater. Sci. Eng., C* **2020**, *112*, 110914.

(22) Wang, Y. Y.; Shahi, P. K.; Wang, X. X.; Xie, R. S.; Zhao, Y.; Wu, M.; Roge, S.; Pattnaik, B. R.; Gong, S. In vivo targeted delivery of nucleic acids and CRISPR genome editors enabled by GSH-responsive silica nanoparticles. *J. Controlled Release* **2021**, *336*, 296−309.

(23) Nazari, F. S. M.; Panahi, H. A.; Jahanmardi, R. Construction of a dual Stimuli-Responsive drug delivery platform based on the copper sulfide nanoparticles modified N-isopropyl Acrylamide/Allyl acetoacetate for docetaxel Delivery: In vitro release and kinetic studies. *Inorg. Chem. Commun.* **2023**, *156*, 111230.

(24) Singh, R. K.; Patel, K. D.; Mahapatra, C.; Parthiban, S. P.; Kim, T.; Kim, H. W. Combinatory Cancer Therapeutics with Nanoceria-Capped Mesoporous Silica Nanocarriers through pH-triggered Drug Release and Redox Activity. *ACS Appl. Mater. Interfaces* **2019**, *11*, 288.

(25) Yang, Z. F.; Wang, L. H.; Liu, Y.; Liu, S. M.; Tang, D. J.; Meng, L.; Cui, B. ZnO capped flower-like porous carbon-Fe$_3$O$_4$ composite as carrier for bi-triggered drug delivery. *Mater. Sci. Eng., C* **2020**, *107*, 110256.

(26) Muhammad, F.; Guo, M. Y.; Qi, W. X.; Sun, F. X.; Wang, A. F.; Guo, Y. J.; Zhu, G. S. pH-Triggered Controlled Drug Release from Mesoporous Silica Nanoparticles via Intracellular Dissolution of ZnO Nanolids. *J. Am. Chem. Soc.* **2011**, *133*, 8778−8781.

(27) Yan, Z. Q.; Zhao, A. D.; Liu, X. P.; Ren, J. S.; Qu, X. G. A pH-switched mesoporous nanoreactor for synergetic therapy. *Nano Res.* **2017**, *10*, 1651−1661.

(28) Rim, H. P.; Min, K. H.; Lee, H. J.; Jeong, S. Y.; Lee, S. C. pH-Tunable Calcium Phosphate Covered Mesoporous Silica Nano-containers for Intracellular Controlled Release of Guest Drugs. *Angew. Chem., Int. Ed.* **2011**, *50*, 8853−8857.

(29) García-Fernández, A.; Aznar, E.; Martínez-Máñez, R.; Sancenon, F. New advances in in vivo applications of gated mesoporous silica as drug delivery nanocarriers. *Small* **2020**, *16* (3), 1902242.

(30) Liu, G. Z.; Wu, J. Z.; Liu, S. Y.; Luan, M. M.; Xu, J.; Wu, Y. J. Tailoring dual drug-backboned polyurethane prodrug nanoparticles as all-in-one nanomedicine for precise multimodal imaging-guided PTT-chemotherapy. *New J. Chem.* **2023**, *47*, 13320−13330.

(31) Oe, E.; Fujisawa, N.; Chen, L.; Uto, K.; Matsumoto, Y.; Ebara, M. Locally implantable nanofibre meshes by sustained release of

(32) Bulatao, B. P.; Nalinratana, N.; Jantaratana, P.; Vajragupta, O.; Rojsitthisak, P.; Rojsitthisak, P. Lutein-loaded chitosan/alginate-coated Fe$_3$O$_4$ nanoparticles as effective targeted carriers for breast cancer treatment. *Int. J. Biol. Macromol.* **2023**, *242*, 124673.

(33) Wen, W.; Wu, L.; Chen, Y.; Qi, X. Y.; Cao, J.; Zhang, X.; Ma, W. J.; Ge, Y. R.; Shen, S. Ultra-small Fe$_3$O$_4$ nanoparticles for nuclei targeting drug delivery and photothermal therapy. *J. Drug Delivery Sci. Technol.* **2020**, *58*, 101782.

(34) Yang, Y. N.; Wan, J. J.; Niu, Y. T.; Gu, Z. Y.; Zhang, J.; Yu, M. H.; Yu, C. Z. Structure-dependent and glutathione-responsive biodegradable dendritic mesoporous organosilica nanoparticles for safe protein delivery. *Chem. Mater.* **2016**, *28*, 9008−9016.

(35) Qi, G. Q.; Wang, S. C.; Yin, Q. Q.; Zhang, Z. C.; Wen, X. C.; Hao, L. G. A pH-Responsive Nanoplatform Based on Magnetic Mesoporous Silica Nanoparticles for Enhanced Treatment of Pancreatic Cancer. *ACS Appl. Nano Mater.* **2023**, *6*, 23184−23195.

(36) Huang, L.; Feng, J.; Fan, W. P.; Tang, W.; Rong, X. X.; Liao, W. J.; Wei, Z. N.; Xu, Y. K.; Wu, A. G.; Chen, X. Y.; Shen, Z. Y. Intelligent pore switch of hollow mesoporous organosilica nano-particles for high contrast magnetic resonance imaging and tumor-specific chemotherapy. *Nano Lett.* **2021**, *21*, 9551−9559.

(37) Dai, Z. D.; Wen, W.; Guo, Z. M.; Song, X. Z.; Zheng, K.; Xu, X. Y.; Qi, X. Y.; Tan, Z. Q. SiO$_2$-coated magnetic nano-Fe$_3$O$_4$ photosensitizer for synergistic tumour-targeted chemo-photothermal therapy. *Colloids Surf., B* **2020**, *195*, 111274.

(38) Fujii, Y.; Zhou, S. J.; Shimada, M.; Kubo, M. Synthesis of Monodispersed Hollow Mesoporous Organosilica and Silica Nano-particles with Controllable Shell Thickness Using Soft and Hard Templates. *Langmuir* **2023**, *39*, 4571−4582.

(39) Dai, L. J.; Liu, M. Y.; Long, W.; Hu, X.; Ouyang, H.; Feng, Y. L.; Deng, F. G.; Wen, Y. Q.; Zhang, X. Y.; Wei, Y. Synthesis of water dispersible and biocompatible nanodiamond composite via photo-catalytic surface grafting of zwitterionic polymers for intracellular delivery of DOX. *Mater. Today Commun.* **2022**, *30*, 103010.

(40) de la Encarnación, C.; de Aberasturi, D. J.; Liz-Marzán, L. M. Multifunctional plasmonic-magnetic nanoparticles for bioimaging and hyperthermia. *Adv. Drug Delivery Rev.* **2022**, *189*, 114484.

(41) Singh, R. K.; Kurian, A. G.; Patel, K. D.; Mandakhbayar, N.; Lee, N. H.; Knowles, J. C.; Lee, J. H.; Kim, H. W. Label-Free Fluorescent Mesoporous Bioglass for Drug Delivery, Optical Triple-Mode Imaging, and Photothermal/Photodynamic Synergistic Cancer Therapy. *ACS Bio Mater.* **2020**, *3*, 2218.

(42) Song, S. H.; Li, X. Y.; Ji, Y. S.; Lv, R. H.; Wu, L.; Wang, H. H.; Cao, M. Z.; Xu, Z. G. GSH/pH dual-responsive and HA-targeting nano-carriers for effective drug delivery and controlled release. *J. Drug Delivery Sci. Tec.* **2021**, *62*, 102327.

(43) Liu, Y. L.; Liang, Y.; Lei, P. P.; Zhang, Z.; Chen, Y. M. Multifunctional Superparticles for Magnetically Targeted NIR-II Imaging and Photodynamic Therapy. *Adv. Sci.* **2023**, *10*, 2203669.

Temozolomide for combined thermo-chemotherapy to treat glioblastoma. *New J. Chem.* **2023**, *47*, 5816−5824.